Journal of the Korean Electrochemical Society
Vol. 6, No. 3, 2003, 187-195

Carbonaceous Materials as Anode Materials for Lithium Ion Secondary Batteries

Seung-Bok Lee and Su-Il Pyun†

Department of Materials Science and Engineering, Korea Advanced Institute of Science and Technology, 373-1 Guseong-Dong, Yuseong-Gu, Daejeon 305-701, KOREA

(Received March 3, 2003 : Accepted April 21, 2003)

Abstract : The present article is concerned with the overview of carbonaceous materials used as anode materials for lithium ion secondary batteries. This article first classified carbonaceous materials into graphite, soft carbon and hard carbon according to their crystal structures, and then summarised the previous works on the characteristics of lithium intercalation/deintercalation into/from the carbonaceous materials. Finally this article reviewed our recent research works on the mechanism of lithium transport through graphite, soft carbon and hard carbon electrodes from the kinetic view point by the analysis of the theoretical and experimental potentiostatic current transients.

Key words : Carbonaceous materials, Lithium intercalation, Numerical simulation, Lithium batteries, Graphite, Soft carbon, Hard carbon

1. Introduction

Graphite is a three dimensional ordered crystal. Soft carbon and hard carbon constructed with two dimensional ordered graphene sheets which are randomly stacked[1,2] have a 'turbo-stractic' structure. Soft carbon is called a graphitizing carbon because it is graphitized by heat-treatment over 2000°C[3]. On the other hand, hard carbon is never graphitized, even at 3000°C under ambient pressure, so it is called a non-graphitizing carbon[4,5]. The raw materials, *i.e*. precursors, usually determine whether the carbon produced is soft or hard carbon. Typical raw materials for soft carbon are such thermoplastic resins as petroleum pitch and coal tar pitch. Hard carbon can be obtained by heat-treatment of such thermosetting resins as phenolic resin and vegetable fibers.

Purified natural graphite and artificial graphite, and soft carbons and hard carbons heat-treated at 1000° to 1400°C have been used as anode materials for lithium ion batteries. Some carbon materials heat-treated below 800°C have a higher capacity than theoretical value (372 mAh/g), but their discharging potential is too high for them to be used in commercial batteries because the voltage of the cell will be lower than 3 V.

This article categorised carbonaceous materials into three types of graphite, soft carbon and hard carbon used as anode materials for lithium ion batteries, and then characterised the respective carbon materials from the view points of lithium intercalation/deintercalation. Finally, this article reviewed the mechanisms of lithium transport through graphite, soft carbon and hard carbon electrodes by the analysis of the potentiostatic current transients theoretically simulated and experimentally measured.

†E-mail: sipyun@webmail.kaist.ac.kr

2. Classification of Carbonaceous Materials

2.1. Graphite and characteristics of lithium intercalation/deintercalation into/from graphite

Graphite materials generally contain polyaromatic rings with sp^2 carbon atoms. These aromatic planar rings are stacked together by π-π interaction of the electronic network[6]. The planar layer formed by the aromatic ring system is generally termed a basal plane. The axis perpendicular to the basal plane is called the C-axis. Two size parameters, namely, the length of the graphite material in the basal plane (L_a) and the length or thickness of the C-axis (L_c) are commonly used to distinguish different types of graphite materials. The schematic diagram of the graphite structure is given in Fig. 1.

The intercalation reaction proceeds via the prismatic surfaces (arm-chair faces and zigzag faces) of the host graphite material[7]. As shown in Fig. 2, during the intercalation reaction the stacking order of the graphene layers in graphite shifts from AB to AA, *i.e*., the intercalated Li guests in LiC_6 are held between two carbon layers directly facing each other.

In LiC_6 the lithium atom is distributed in-plane in such a manner that it avoids the occupation of nearest neighbor sites. A higher lithium in-plane density by occupation of nearest neighbor sites is obtained in the phases LiC_2 and LiC_4, which are prepared chemically from graphitic carbon under high pressure (≈ 60 kbar) and temperature (≈ 3000°C) conditions[8,9]. The close Li-Li distance in LiC_2 results in a higher chemical activity of lithium atom than that of lithium metal (Li-Li bond length (20°C) = 0.304 nm)[10]. Under ambient conditions LiC_2 decomposes slowly via different metastable intermediate Li/C phases to LiC_6 and metallic lithium.

The term 'stage' in graphite intercalation compounds (GIC) essentially refers to the number of graphite layers that lie

between alternate intercalant layers. Hence, stage 1 is the GIC system with the highest level of intercalant concentration. The staging phenomenon can be easily monitored and controlled by the electrochemical methods. Two basic methods which have proved to be practically useful are galvanostatic and potentiostatic methods. Fig. 3 shows a schematic potential/composition curve for the galvanostatic reduction of graphite to $Li_\delta C_6$.

The distinguishable plateau on the potential curve indicates two-phase regions in the lithium/graphite phase diagram. Assuming that the current yield is 100%, one can analyse phases and determine the stoichiometry "δ" for the individual stages $Li_\delta C_6$. Apart from stage 1, four other binary phases $Li_\delta C_6$ corresponding to the stage 4, stage 3, stage 2L and stage 2 (which can also be obtained by chemical synthesis) were characterised by these methods. X-ray[11] and Raman[12] measurements confirm the results.

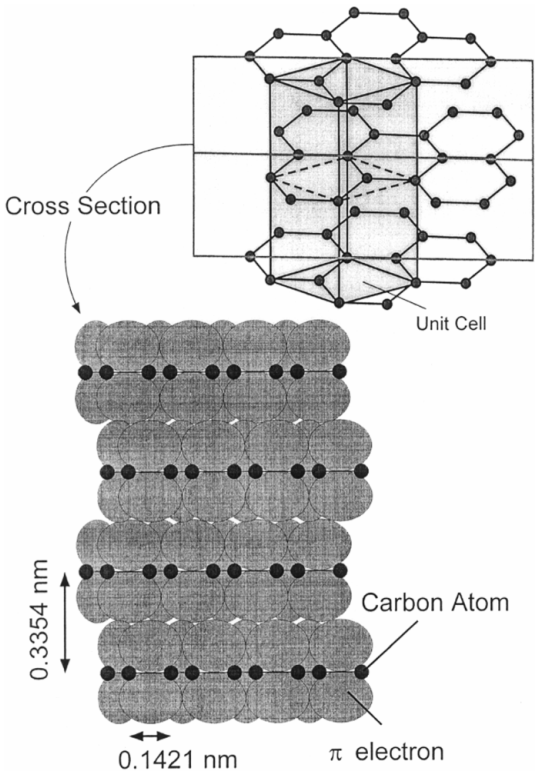

Fig. 1. Structure of hexagonal graphite showing ABAB stacking, and schematic diagram of cross-section of stacking layers considering the thickness of each carbon layer.

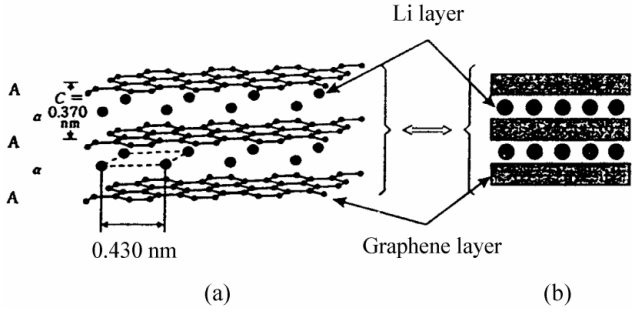

Fig. 2. Schematic diagram (a) showing graphite AA-layer stacking and lithium intercalate αα interlayer ordering, and (b) showing simplified schematic representation.

2.2. Soft carbon and characteristics of lithium intercalation/deintercalation into/from soft carbon

Soft carbons are carbon materials whose structure evolves progressively toward the graphite structure when they are heat-treated at high temperature, up to 3000°C[13]. They consist of more or less misoriented crystallites whose sizes and crystalline order increase with the heat-treatment temperature (HTT). The schematic diagram of soft carbon structure is given in Fig. 4. At the beginning of the graphitization step (HTT of 1200-1300°C), the size of the crystallites is of the order of 5 nm, both parallel and perpendicular to the layers (L_a and L_c, respectively), with an average interplane distance d_{002} close to 0.344 nm. The crystallite size is about 10 nm at HTT of 2000°C and reaches several ten nm with higher HTTs, while d_{002} approaches that value of graphite (0.3354 nm). Typical soft carbons are graphitizable cokes, ex-mesophase

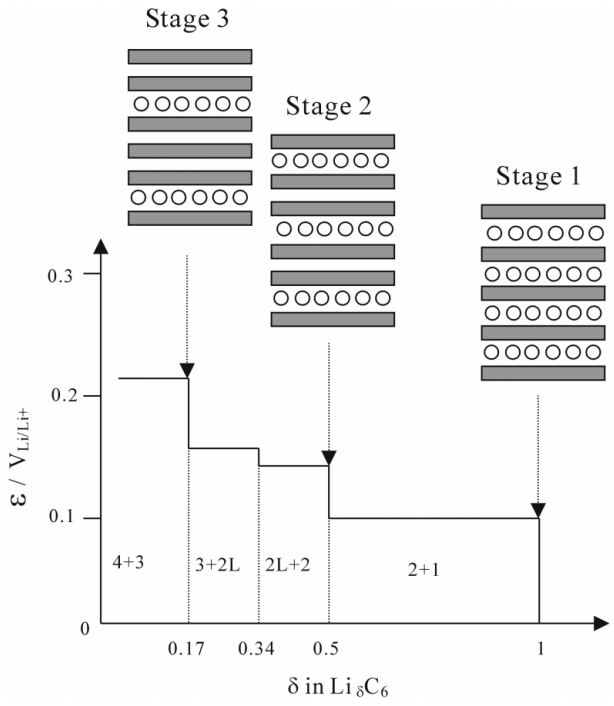

Fig. 3. Electrochemical lithium intercalation with stage formation.

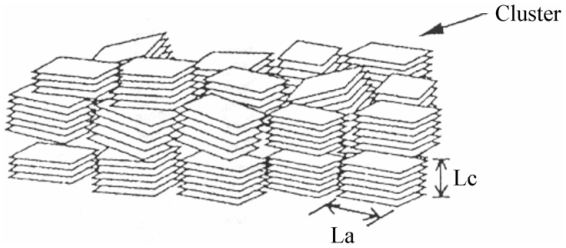

Fig. 4. Schematic diagram of the structure of soft carbon.

carbon fibers, vapour-grown carbon fibers and mesocarbon-microbeads (MCMB)[14].

As shown in Fig. 5, all heat-treated soft carbons showed two domains of electrochemical behaviour according to whether the heat-treatment temperature (HTT) is higher or lower than 2000°C[15]. It has been known that this value of HTT is a critical value for the behaviour of numerous physical and structural properties. It corresponds to a sharp increase in three dimensional ordering, which is evidenced by analysis of the X-ray diffraction patterns. The increase of reversible capacities above HTT of 2000°C can therefore be understood from the increased crystallinity. However, the capacity increase at low HTT is unexpected. High capacities have been observed for carbon materials prepared from organic pyrolyzed at low temperatures (700°-1000°C).

It was report that the minimum capacity occurs when L_c is of the order of 10 nm[16]. For $L_c > 10$ nm, a classical intercalation process should occur[17,18]. On the other hand, for $L_c <$ 10 nm, the authors assumed the occurrence of a different process of doping and undoping, namely the formation of covalent Li_2 molecules which could act as a Li ion reservoir. They reported that such a process would be enhanced by decreasing the crystallite thickness.

Another explanation was proposed by Dahn *et al.*[15,19] Their model is based on Franklin's model of graphitization, in which a pregraphitic carbon is seen as a mixture of organized and unorganized regions. Organized regions would be constituted of parallel carbon layers either registered in ABAB stacking as in graphite or turbostratic, *i.e.* with random shifts or rotations between them. The unorganized regions would consist of groups of tetrahedrally bonded carbon atoms or highly buckled graphitic sheets.

Dahn *et al.*[15,19] were also able to determine the relative amounts of registered, turbostratic and unorganized layer in a given pregraphitic carbon from the analysis of X-ray data. Assuming that the amount of Li which six carbon atoms can accommodate is 1 for registered layer, 0.9 for unorganized layers and 0.25 (HTT < 2200°C) or 0.00 (HTT > 2200°C) for turbostratic layers, they could fit the dependence of reversible capacities on HTT. Thus, they reported that turbostratic disorder would not play the same role according to whether HTT is higher or lower than 2200°C. For HTT > 2200°C, the interlayer spaces or galleries between randomly stacked layers would not accommodate lithium atoms and these 'blocked' galleries would frustrate the formation of the regular sequence of full and empty galleries (staged phases).

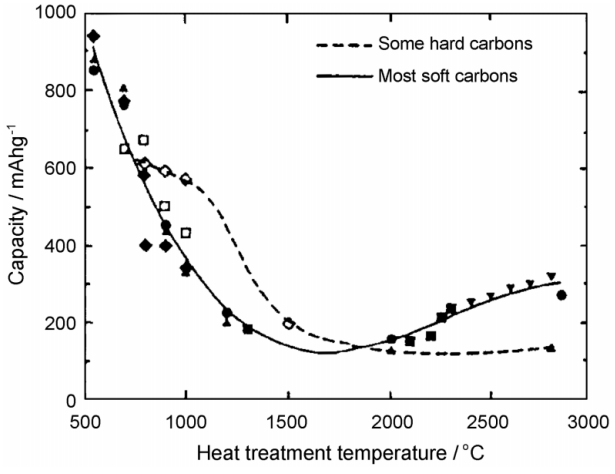

Fig. 5. Relationship between reversible specific capacity and heat-treatment temperature of various soft carbons and hard carbons[15].

Mochida *et al.*[20] reported that there exist four kinds of lithium deintercalation sites within soft carbon heat-treated below about 1000°C such as charge transferring surface site, intercalation site between graphene layers, zigzag site in edge plane and finally armchair site in edge plane, which are designated as the site for Type I, Type II, Type III-1 and Type III-2, respectively. Moreover, the potential necessary for lithium deintercalation from the sites for Type I, Type II, Type III-1 and Type III-2 ranges between 0.25 and 1.5 $V_{Li/Li+}$, 0 and 0.25 $V_{Li/Li+}$, 0 and 0.10 $V_{Li/Li+}$, and 0.10 and 0.40 $V_{Li/Li+}$, respectively.

As detailed above, generally accepted coincidence has not yet been reached on the mechanism of lithium transport through the soft carbon electrode, since the carbonaceous materials have very complex and various microstructures according to the heat-treatment temperature and precursor.

2.3. Hard carbon and characteristics of lithium intercalation/deintercalation into/from hard carbon

Hard carbon has such physical properties as non-graphitizability, low density and large shrinkage at the calcinations. The schematic diagram of hard carbon structure is given in Fig. 6. It has been recently reported that hard carbons heat-treated at temperatures in a limited range around 1000°C[21,22] have much higher capacities than the theoretical capacity of graphite. The hard carbons are promising materials and have attracted much attention of many researchers for use as anodes in high-capacity lithium ion cells in the near future.

One of the characteristic features of hard carbons is the hysteresis of their charge and discharge profiles. In other words, lithium atom is intercalated near 0 $V_{Li/Li+}$, but deintercalated at about 1 $V_{Li/Li+}$. Although hard carbons show high reversible capacities, their low density (ca. 1.5 g/cm^3), low coulombic efficiency (50-60%) at the first cycle, and poor

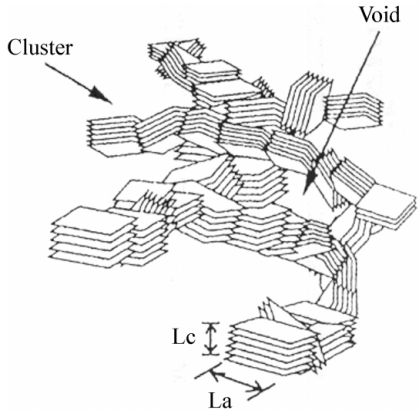

Fig. 6. Schematic diagram of the structure of hard carbon.

re-chargeability remained to be solved before use in practical cells. In addition, the hysteresis of the potential profile is one of the disadvantages of hard carbons because it causes a substantial energy loss.

Since their reversible capacity values are much higher than the theoretical capacity of graphite, the insertion mechanism can not be explained by the simple model that lithium atom is intercalated between carbon layers. Various models for high capacity carbons in hard have been suggested so far. Sato *et al.*[23] analysed their pyrolyzed poly (p-phenylene) (PPP) using ^{7}Li-NMR. Their carbon had a high capacity of 680 mAh/g, and showed two different NMR peaks when lithium atom is inserted. They assigned the two peaks to ionic Li species and covalent Li_2 molecules, and suggested a mechanism where lithium atom is inserted between carbon layers with an in-plane LiC_2 structure. Carbons heat-treated below 1000°C contain significant amounts of residual hydrogen atoms. As for the mechanism of lithium intercalation (or doping) into the high hydrogen-containing carbons (H/C atomic ratio ≥ 0.05), it is much more complex mainly because there exist heteroatoms, *i.e.* hydrogen etc., in those carbons.

Dahn *et al.*[24,25] argued that it is very difficult for lithium atom to occupy the nearest neighbor sites between graphene sheets at ambient temperature and normal pressure. Moreover, Sato *et al.*'s[23] model can not explain the large hysteresis in the charge-discharge potential profile. They believed that upon the lithium intercalation, lithium atom can bind hydrogen atom and can transfer part of its 2s electron to a nearby hydrogen atom, resulting in a corresponding change to a H-C bond from sp^2 to sp^3. Upon the lithium deintercalation, the reverse process happens, and there is a difference in the activation energy between for the lithium intercalation and for the lithium deintercalation mentioned above, so the large hysteresis between the charge-discharge profiles is observed. Unfortunately, there is insufficient evidence to prove this model and further work is needed to ascertain how the inserted lithium atom is attached to nearby hydrogen atom.

The potential profile of hard carbon is quite different from that of the soft carbons, which implies that the mechanism for lithium doping is also different. Dahn *et al.*[24] have also proposed a 'surface adsorption' model to explain the mechanism of lithium intercalation into hard carbons, which assume that the lithium atom is weakly bound on the pore surfaces, therefore, no potential hysteresis is expected in the charge-discharge potential profile. Furthermore, Dahn *et al.*[22] showed that these carbon materials consist primarily of small single layers of carbon like a "house of cards", and proposed that lithium atom could be adsorbed on both of the surfaces of these single layers, which leads to a higher capacity than that of graphite.

Moreover, it was reported by Mochida *et al.*[20] that there exist four kinds of lithium deintercalation sites within hard carbon such as charge transferring surface site, intercalation site between graphene layers, cluster gap between edge planes and finally microvoid surrounded by hexagonal planes, which are designated as the site for Type I, Type II, Type III and Type IV, respectively. In addition, the potential necessary for lithium deintercalation from the sites for Type I, Type II, Type III and Type IV ranges between 0.25 and 2.00 V_{Li/Li^+}, 0 and 0.25 V_{Li/Li^+}, 0 and 0.10 V_{Li/Li^+}, and 0 and 0.13 V_{Li/Li^+}, respectively.

For practical use as anode of lithium ion batteries, however, the discharge potential of hard carbon (approaching $1V_{Li/Li^+}$ *i.e.*, large hysteresis), charge potential (close to 0 V_{Li/Li^+} which may cause lithium metal deposition) of hard carbon and the low density of hard carbon materials are meeting some difficulties.

3. Kinetics of Lithium Transport through Carbonaceous Materials

Until now we classified the carbonaceous materials according to their structure into three types and summarised the lithium intercalation/deintercalation characteristics proposed by many researchers. Now we reviewed our recent works on kinetics of lithium transport though graphite[26], soft carbon[27,28] and hard carbon[29] electrodes by the analysis of current transients.

3.1. Lithium transport through graphite electrode

Fig. 7 gives the electrode potentials obtained from the galvanostatic intermittent discharge curve of the SFG6 graphite composite electrode in a 1 M $LiPF_6$-EC/DEC solution as a function of intercalated lithium content. The electrode potential curve displayed three 'potential plateaux' near 0.10 V_{Li/Li^+}, 0.13 V_{Li/Li^+} and 0.22 V_{Li/Li^+}, which proved to stem from the equilibrium coexistences of two different stages as designated in this figure.

Fig. 8 illustrates on a logarithmic scale the anodic current transients experimentally measured on the SFG6 graphite composite electrode in a 1 M $LiPF_6$-EC/DEC solution. The current transients were measured by jumping the electrode

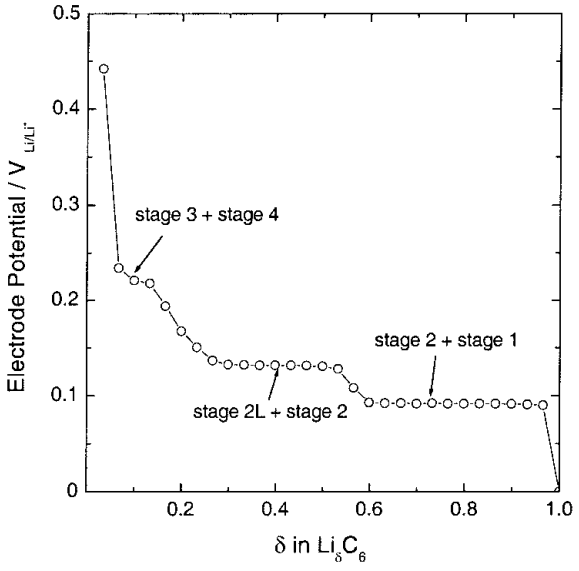

Fig. 7. The galvanostatic intermittent discharge curve obtained from the SFG6 graphite composite electrode in a 1 M $LiPF_6$-EC/DEC solution.

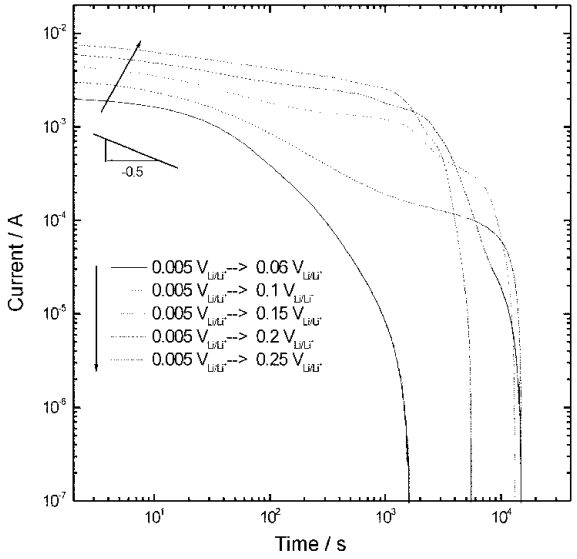

Fig. 8. The anodic current transients experimentally measured on the SFG6 graphite composite electrode in a 1M $LiPF_6$-EC/DEC solution at the applied potential jumps from 0.005 V_{Li/Li^+} to various lithium extraction potentials in the range of 0.06 to 0.25 V_{Li/Li^+}.

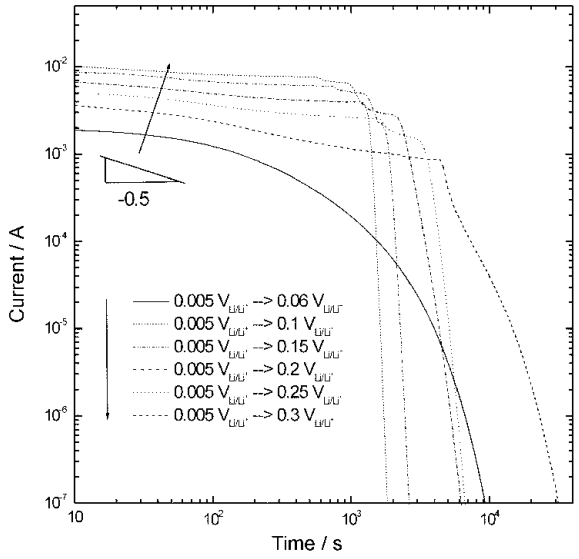

Fig. 9. The anodic current transients at the applied potential jump from 0.005 V_{Li/Li^+} to various lithium extraction potentials in the range of 0.06 to 0.25 V_{Li/Li^+}, theoretically determined by means of numerical analysis based upon the 'cell-impedance-controlled' constraint at the interface between electrolyte and electrode of cylindrical symmetry, and impermeable constraint on the central axis of the cylindrical particle of the electrode.

potential from 0.005 V_{Li/Li^+} to various lithium extraction potentials in the range of 0.06 to 0.25 V_{Li/Li^+}. The absolute values of the slopes of all the logarithmic current transients increased monotonically with time in the initial stage of the current transients; the linear relationship with the slope of -0.5 on a logarithmic scale (the Cottrell behavior) was never followed. This strongly suggests that the anomalous current transient is responsible for the 'cell-impedance-controlled' lithium transport.

The current transients were modeled based upon the Fick's diffusion equation as a governing equation in combination with the 'cell-impedance-controlled' boundary condition as follows:

$$\text{I.C.: } c = c_0 \text{ for } 0 \le r \le R^* \text{ at } t = 0 \quad (1)$$

$$\text{B.C.: } zFA_{ea}\tilde{D}_{Li^+}\left|\frac{\partial c}{\partial r}\right| = \frac{|E - E_{app}|}{R_{cell}} \text{ for } r = R^* \text{ at } t > 0 \quad (2)$$

('cell-impedance-controlled' constraint)

$$zFA_{ea}\tilde{D}_{Li^+}\left(\frac{\partial c}{\partial r}\right) = 0 \text{ for } r = 0 \text{ at } t \ge 0 \quad (3)$$

(impermeable boundary condition)

where c is the local concentration of lithium; r, the distance from the center of the graphite particle; R^*, the average radius of the graphite particle; E, the electrode potential; E_{app}, the applied potential; R_{cell}, 'cell-impedance'; z, the valence number of lithium ion; F, the Faraday constant; A_{ea}, the electrochemical active area, $\tilde{D}_{Li^+}$ represents the chemical diffusivity of lithium.

Fig. 9 shows on a logarithmic scale the anodic current transients determined from numerical solution to the Fick's diffusion equation for the conditions of Eqs. (1)-(3) by taking the values described above. The calculated current transients (Fig. 9) shared the corresponding experimental current transients (Fig. 8) in value and shape, with regard to the non-Cottrell character and Ohmic behavior between the applied potential step and initial current level. These results strongly indicate that lithium transport through the graphite electrode in a 1 M $LiPF_6$-EC/DEC solution is governed by the 'cell-impedance-controlled' constraint during the whole lithium transport.

3.2. Lithium transport through soft carbon electrode

Fig. 10 shows powder XRD patterns obtained from the MCMB heat-treated at various temperatures of 800° to 1200°C. Three broad diffraction peaks were observed near 25°, 43° and 78°, which correspond to (002), (100) and (110) planes, respectively. This means that the heat-treated MCMB powders still have low degree of crystallinity by heat-treatment up to 1200°C. That is to say, the size of the microcrysallite in the a- and c-axis direction, *i.e.*, L_a and L_c, still have small value at heat-treatment temperatures up to 1200°C.

Fig. 11 presents electrode potentials obtained from the galvanostatic intermittent discharge curves measured on the PVDF bonded-MCMB800, MCMB1000, and MCMB1200 composite electrodes in 1 M $LiPF_6$-EC/DEC solution as a function of intercalated lithium content. All the electrode potential curves did not show any 'potential plateau', rather they ran continuously throughout the whole lithium deintercalation. This means that the MCMB heat-treated below 1200°C still has a very low degree of crystallinity, and hence lithium is deintercalated from the MCMB particles without formation of any thermodynamically stable phases.

Figs. 12(a)-(c) give on a logarithmic scale the anodic current

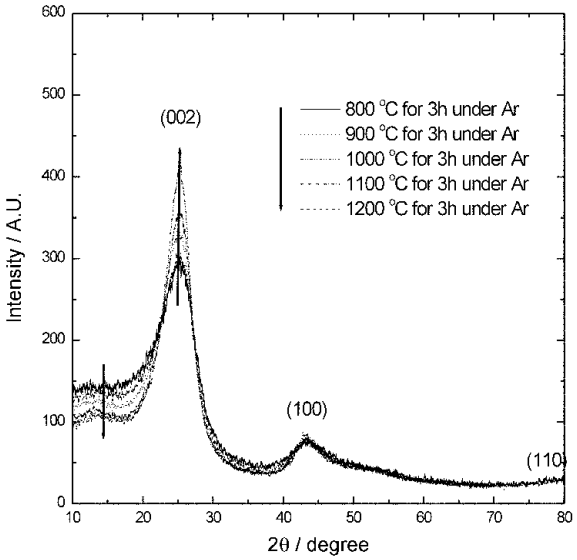

Fig. 10. XRD patterns measured on the MCMB powders heat-treated at various temperatures.

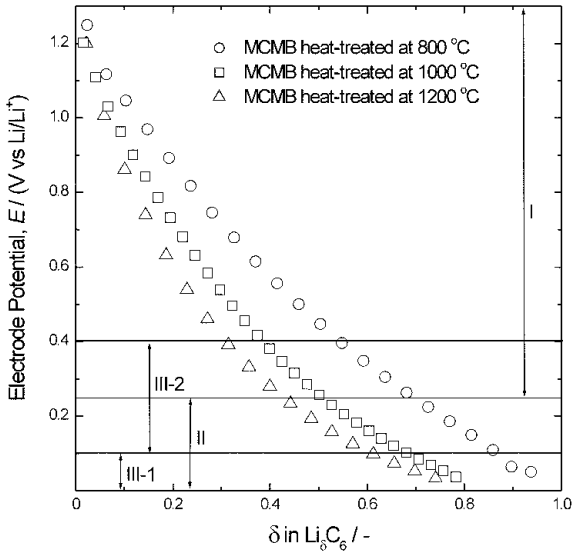

Fig. 11. The galvanostatic intermittent discharge (electrode potential) curve measured on the PVDF-bonded MCMB800(○), MCMB1000(□) and MCMB1200(Δ) composite electrodes in 1 M $LiPF_6$-EC/DEC solution. Region I, II, III-1 and III-2 represent the potential ranges necessary for lithium deintercalation from the sites for Type I, Type II, Type III-1 and Type III-2, respectively.

transients, experimentally obtained from the PVDF-bonded MCMB800 composite electrode in 1 M $LiPF_6$-DC/DEC solution. The anodic current transients were measured at the potential jumps 0.05, 0.2 and 0.3 V_{Li/Li^+} to various lithium extraction potentials.

From the analysis of the current transients, it was elucidated that lithium transport through the soft carbon electrode is also governed by the 'cell-impedance-controlled' constraint. It is generally accepted that an inflexion point, *i.e.*, 'quasi-current plateau' should be necessarily observed in the current

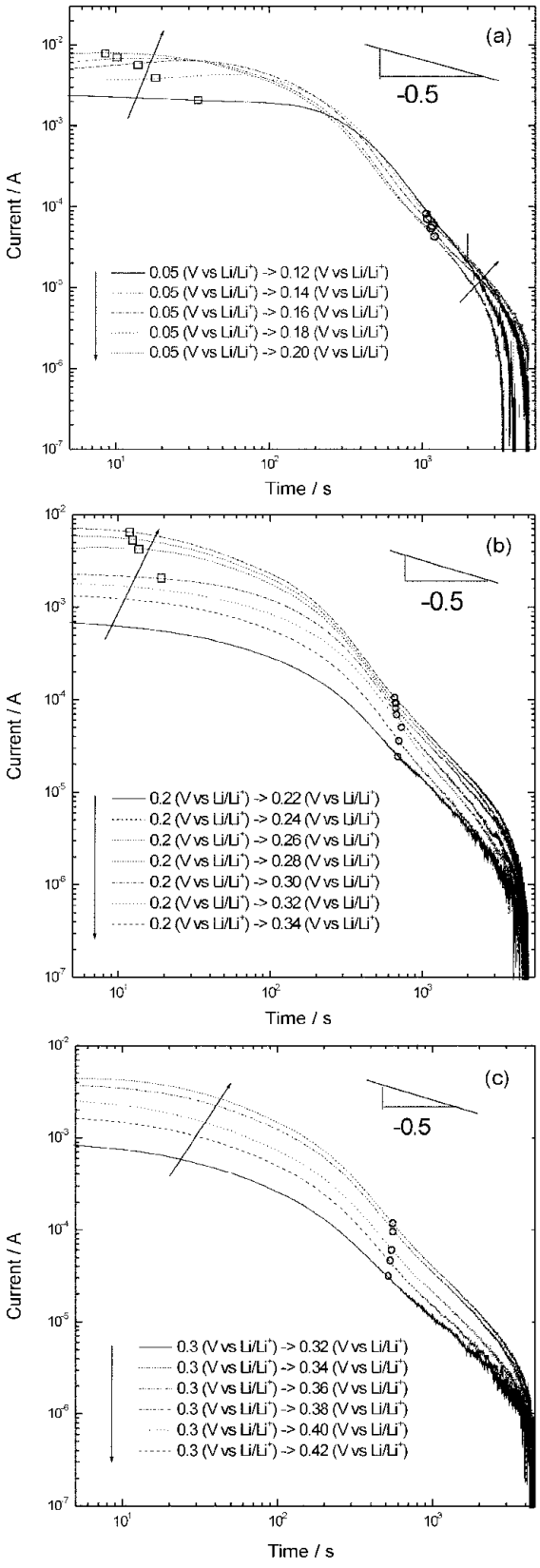

Fig. 12. The anodic current transient experimentally obtained from the PVDF-bonded MCMB800 composite electrode in 1 M $LiPF_6$-EC/DEC solution at the potential jumps of E = (a) 0.05 V_{Li/Li^+}, (b) 0.20 V_{Li/Li^+} and (c) 0.30 V_{Li/Li^+} to various lithium extraction potentials E_{ext} as indicated in figure. Symbols □ and ○ denote inflexion points.

transient, only when a 'potential plateau' indicating the coexistence of two phases appears in the electrode potential curve under the 'cell-impedance-controlled' constraint[30]. However, the current transients of Figs. 12(a)-(c) showed inflexion point even though the electrode potential curve measured on the electrode did not show any potential plateau throughout the whole lithium intercalation/deintercalation.

In the work, this abnormal current transient behaviour involving the inflexion point could be reasonably explained in terms of the difference in the kinetics of lithium deintercalation from two different lithium deintercalation sites having different activation energies for lithium deintercalation.

Thus, the McNabb-Foster equation[27-29,31,32] was modified to satisfy spherical symmetry and to represent the coexistence of two different kinds of trap sites, and it was used as a governing equation for lithium transport as follows

$$\tilde{D}_{Li}\left[\frac{2}{R^*}\left(\frac{\partial c}{\partial r}\right)+\frac{\partial^2 c}{\partial r^2}\right]=\frac{\partial c}{\partial t}+N_I\frac{\partial \theta_I}{\partial t}+N_{II}\frac{\partial \theta_{II}}{\partial t} \quad (4)$$

with the rate of reversible trapping into and escaping from the trap sites described by

$$\frac{\partial \theta_I}{\partial t} = k_I c(1-\theta_I)-p_I\theta_I \quad (5)$$

$$\frac{\partial \theta_I}{\partial t} = k_{II} c(1-\theta_{II})-p_{II}\theta_{II} \quad (6)$$

where t is the deintercalation time; N_I and N_{II}, the concentrations of the trap sites of I and II, respectively; θ_I and θ_{II}, the occupancy fractions of the trap sites of I and II, respectively; k_I and k_{II}, the capture rates into the trap sites of I and II, respectively; p_I and p_{II} represent the release rates from the trap sites of I and II, respectively. And, as the initial condition (I.C.) and the boundary conditions (B.C.), Eq. (1) and Eqs. (2)-(3) were used, respectively.

From the numerical solution to the modified McNabb-Foster equation, the anodic current transients at the potential jumps of 0.05, 0.2, and 0.3 V_{Li/Li^+} to various lithium extraction potentials E_{ext} were determined, and they are illustrated in Figs. 13(a)-(c). The anodic current transients theoretically calculated based upon the modified McNabb-Foster equation along with the 'cell-impedance-controlled' constraint of Figs. 13(a)-(c) almost coincided with those current transients experimentally measured of Figs. 12(a)-(c) in value and in shape. This strongly indicates that the appearance of an inflexion point in the current transient is due to the lithium deintercalation from two different kinds of deintercalation sites with clearly distinguishable activation energies.

3.3. Lithium transport through hard carbon electrode

Fig. 14 presents electrode potentials obtained from the galvanostatic intermittent discharge curve in a 1 M $LiPF_6$-EC/DEC solution as a function of intercalated lithium content. At the same time, the potential ranges necessary for lithium deintercalation from the four different lithium deintercalation

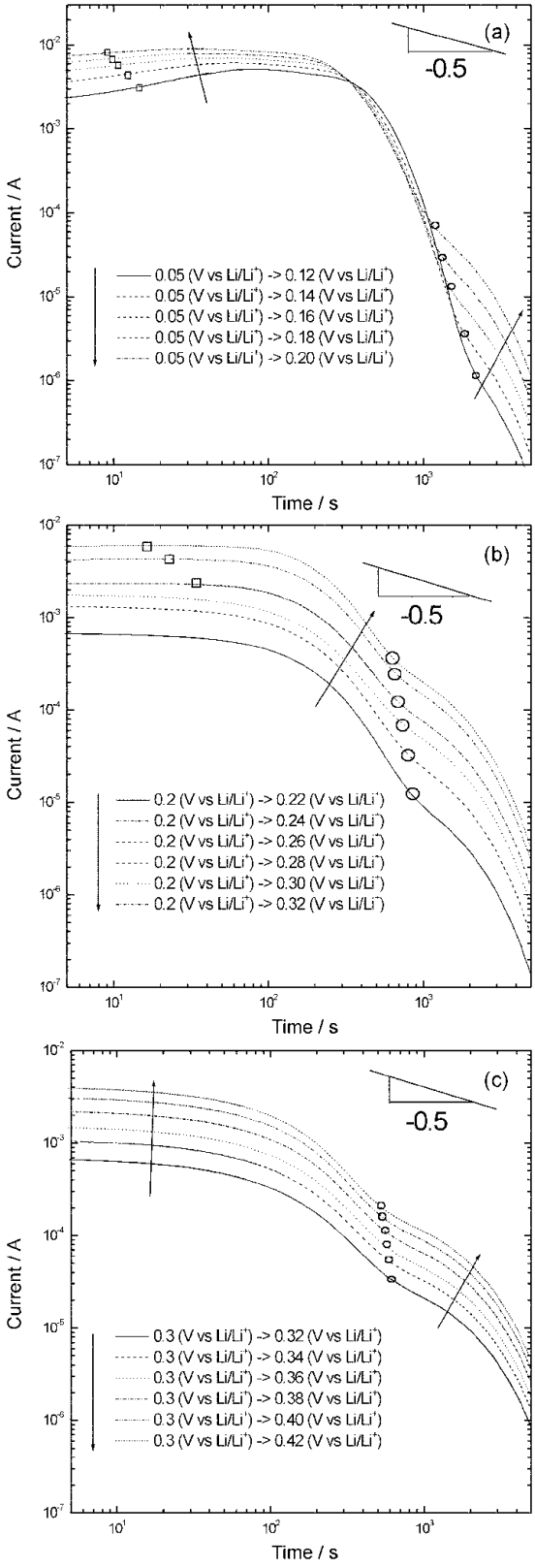

Fig. 13. The anodic current transient theoretically calculated based upon the modified McNabb-Foster equation at the potential jumps of E = (a) 0.05 V_{Li/Li^+}, (b) 0.20 V_{Li/Li^+} and (c) 0.30 V_{Li/Li^+} to various lithium extraction potentials E_{ext} under the 'cell-impedance-controlled' constraint, by taking A_{eq} = 1.56 cm^2, $\tilde{D}_{Li}$ = 2×10^{-10} cm^2s^{-1}, R_{cell} = 27.8 Ω and R^* = 5 μm. Symbols □ and ○ denote inflexion points.

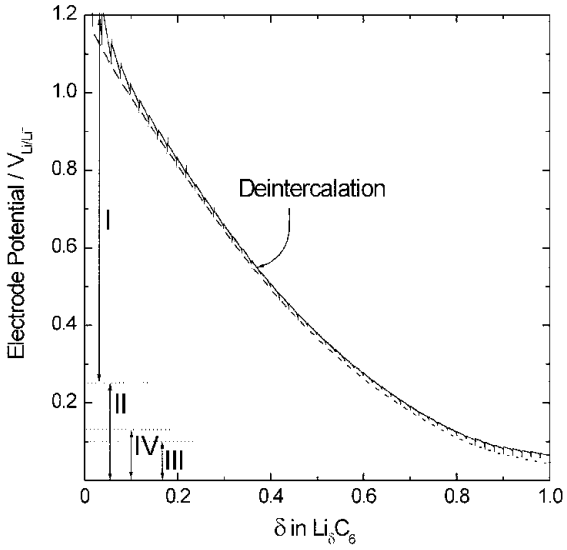

Fig. 14. The galvanostatic intermittent discharge curve measured on the Carbotron-P hard carbon composite electrode in a 1 M $LiPF_6$-EC/DEC solution. Region I, II, III and IV represent the potential ranges necessary for lithium deintercalation from the sites for Type I, Type II, Type III and Type IV, respectively.

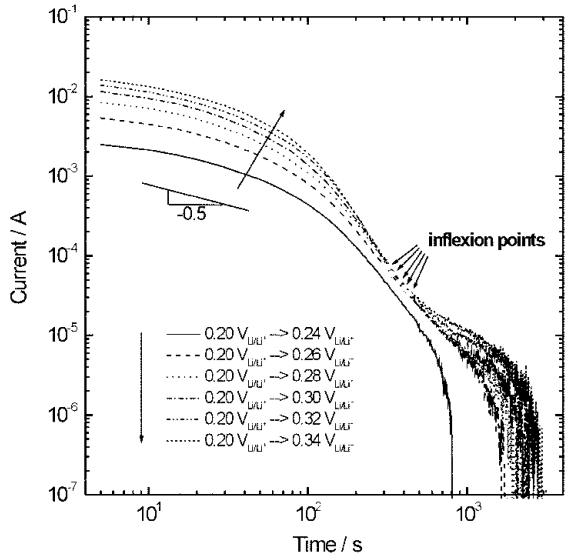

Fig. 15. The anodic current transients experimentally measured on the Carbotron-P hard carbon composite electrode in a 1 M $LiPF_6$-EC/DEC solution by jumping the initial electrode potential 0.20 V_{Li/Li^+} to various lithium extraction potentials as indicated in figure.

sites within hard carbon proposed by Mochida[20] are also given in this figure. The electrode potential curve did not show any 'potential plateau', rather it ran continuously throughout the whole lithium deintercalation. This means that the Carbotron-P powder has a very low degree of crystallinity, and hence lithium is deintercalated from Carbotron-P particles without formation of any thermodynamically stable phases.

Fig. 15 envisages on a logarithmic scale the anodic current transients experimentally measured by jumping the initial electrode potential 0.20 to various lithium extraction potentials. In the previous work, lithium transport through hard carbon electrode is also governed by the 'cell-impedance-controlled' constraint. The shape of the current transient measured at the potential jump of 0.20 to 0.24 V_{Li/Li^+}, was somewhat different from those measured at the potential jumps of 0.20 to various lithium extraction potentials 0.26 to 0.34 V_{Li/Li^+}. The former current transient showed the two-stage current transient behaviour. By contrast, the latter current transients showed a three-stage current transient behaviour, which is characterised by the presence of an inflexion point, *i.e.*, a 'quasi-current plateau'.

Similar to the case of soft carbon electrode, the anodic current transients measured on the hard carbon electrode clearly showed an inflexion point, *i.e.*, a 'current plateau' even though the electrode potential curve did not show any 'potential plateau' throughout the whole lithium deintercalation. In the work, such an abnormal current transient behaviour showing the 'inflexion point' at the Carbotron-P hard carbon composite electrode could be reasonably analysed in terms of the difference in activation energies for lithium deintercalation by employing McNabb-Foster equation and 'cell-impedance controlled' constraint as governing equation and boundary condition, respectively.

The simulated current transients by jumping the initial electrode potential 0.20 to various lithium extraction potentials determined from the numerical solution to the modified McNabb-Foster equation were illustrated in Fig. 16. The anodic current transient at the potential jump of 0.20 to 0.24 V_{Li/Li^+} showed the two-stage current transient behaviour, *i.e.* a monotonic decrease in logarithmic current with logarithmic time, followed by an exponential decay. However, those current transients at the potential jumps of 0.20 V_{Li/Li^+} to the lithium extraction potentials 0.26 to 0.34 V_{Li/Li^+} exhibited an

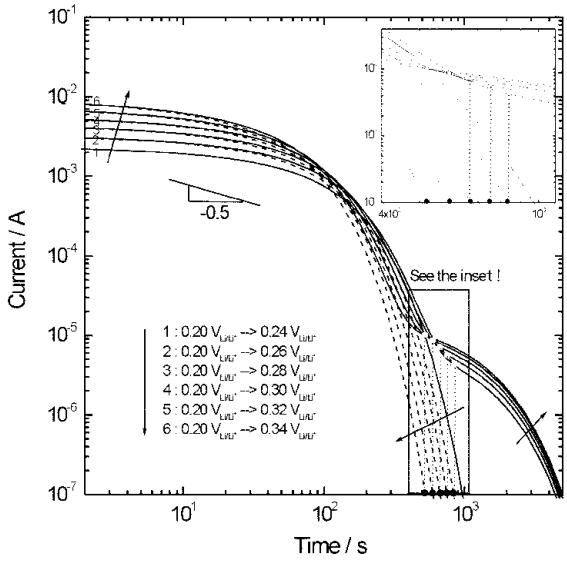

Fig. 16. The anodic current transients theoretically calculated based upon the modified McNabb-Foster equation (solid line) and calculated under the assumption of lithium ion transport through a single phase in the absence of any trap sites (dashed line) at the potential jumps of 0.20 V_{Li/Li^+} to various lithium extraction potentials under the 'cell-impedance-controlled' constraint, by taking A_{ea} = 13 cm^2, $\tilde{D}_{Li}$ = 8×10^{-9} cm^{2}s^{-1}, R_{cell} = 15.2 Ω and R^* = 5 μm.

inflexion point, *i.e.*, a 'quasi-current plateau'.

The anodic current transients theoretically calculated based upon the modified McNabb-Foster equation along with the 'cell-impedance-controlled' constraint of Fig. 16 almost coincided with those current transients experimentally measured of Fig. 15 in value and in shape. This strongly suggested that lithium transport through the Carbotron-P hard carbon composite electrode is governed by 'cell-impedance', and at the same time the difference in activation energies for lithium deintercalation between from the four different lithium deintercalation sites existing within the electrode is responsible for the different kinetics of lithium transport between through the four different lithium deintercalation sites, which leads to the presence of the inflexion points, *i.e.*, 'quasi-current plateaux' in the current transients.

4. Conclusion

This article first categorised carbonaceous materials into three types of graphite, soft carbon and hard carbon, depending upon their crystal structures, and then summarised the previous works on the characteristics of lithium intercalation/deintercalation into/from the carbonaceous materials. Finally this article reviewed our recent research works on mechanism of lithium transport through graphite, soft carbon and hard carbon electrodes from the kinetic view point by the analysis of the potentiostatic current transients theoretically calculated and experimentally determined. In our recent works, it was found that the lithium transport through the carbonaceous materials is governed by the 'cell-impedance-controlled' constraint, and at the same time the difference in activation energies for lithium deintercalation between from the four different lithium deintercalation sites existing within the electrode is responsible for the different kinetics of lithium transport between through the four different lithium deintercalation sites, which leads to the presence of the inflexion points, *i.e.*, 'quasi-current plateaux' in the current transients.

Acknowledgement

This work was partly supported by the Brain Korea 21 Project.

References

1. T. Ohzuku, Y. Iwakoshi and K. Sawai, *J. Electrochem. Soc*., **140**, 2490 (1993).
2. Y. Ein-Eli, *Electrochem. Solid State Letters*, **2**, 212 (1999).
3. I. Mochida, C. -H. Ku, S. -H. Yoon and Y. Korai, *J. Power Sources*, **75**, 214 (1998).
4. Y. H. Liu, J. S. Xue, T. Zheng and J. R. Dahn, *Carbon*, **34**, 193 (1996).
5. Y.-J. Kim, H.-J. Yang, S.-H. Yoon, Y. Korai, I. Mochida, C.-H. Ku, *J. Power Sources*, **113**, 157 (2003).
6. H. Azuma, H. Imoto, S. Yamada and K. Sekai, *J. Power Sources*, **81-82**, 1 (1999).
7. T. Tran and K. Kinoshita, *J. Electroanal. Chem.*, **386**, 221 (1995).
8. V. A. Nalimova, D. Guerard, M. M. Lelaurain and O. V. Fateev, *Carbon*, **33**, 177 (1995).
9. V. A. Nalimova, C. Bindra and J. E. Fisher, *Solid State Commun.*, **97**, 583 (1996).
10. D. R. Lide (Ed.), "Handbook of Chemistry and Physics", 75th Edition, CRC Press (1994).
11. D. Billaud, F. X. Henry and P. Willmann, *Mat. Res. Bulletin*, **28**, 477 (1993).
12. M. Inaba, H. Yoshida, Z. Ogumi, T. Abe, Y. Mizutani and M. Asano, *J. Electrochem. Soc.*, **142**, 20 (1995).
13. Y. Nishi, *Mol. Cryst. Liq. Cryst.*, **340**, 419 (2000).
14. Z. Ogumi and M. Inaba, *Bull. Chem. Jpn.*, **71**, 521 (1998).
15. J. R. Dahn, A. K. Sleigh, H. Shi, J. N. Reimers, Q. Zhong and B. M. Way, *Electrochim. Acta*, **38**, 1179 (1993).
16. M. Endo, Y. Nishimura, T. Takahashi, K. Takeuchi and M. S. Dresselhaus, *J. Phys. Chem. Solids*, **57**, 725 (1996).
17. M. Inagaki, N. Iwashita and Y. Hishiyama, *Mol. Cryst. Liq. Cryst*, **244**, 89 (1994).
18. N. Iwashita, M. Inagaki and Y. Hishiyama, *Carbon*, **35**, 1073 (1997).
19. T. Zheng and J. R. Dahn, *Phys. Rev. B*, **53**, 3061 (1996).
20. I. Mochida, C.-H. Ku and Y. Korai, *Carbon*, **39**, 399 (2001).
21. Y. Liu, J. S. Xue, T. Zheng and J. R. Dahn, *Carbon*, **34**, 193 (1996).
22. W. Xing, J. S. Xue, T. Zheng, A. Gibaud and J. R. Dahn, *J. Electrochem. Soc*., **143**, 3482 (1996).
23. K. Sato, M. Noguchi, A. Demachi, N. Oki and M. Endo, *Science*, **264**, 556 (1994).
24. J. R. Dahn, T. Zheng, Y. Liu and J. S. Xue, *Science*, **270**, 590 (1995).
25. T. Zheng, W. R. McKinnon, and J. R. Dahn, *J. Electrochem. Soc.*, **143**, 2137 (1996).
26. S.-I. Pyun, S.-B. Lee and W.-Y. Chang, *J. New Mater. Electrochem. System*, **5**, 281 (2002)
27. S.-B. Lee and S.-I. Pyun, *Electrochim. Acta*, **48**, 419 (2002).
28. S.-B. Lee and S.-I. Pyun, *J. Solid State Electrochem.*, **7**, 374 (2003).
29. W.-Y. Chang, S.-I. Pyun and S.-B. Lee, *J. Solid State Electrochem.*, **7**, 368 (2003).
30. H.-C. Shin and S.-I. Pyun, in: White RE, Conway BE, Vayenas CG (eds), "Modern Aspects of Electrochemistry", Number 36. Plenum Publishers, New-York, pp 255-301 (2003).
31. A. McNabb and P. K. Foster, *Trans. Met. Soc. AIME*, **227**, 618 (1963).
32. S.-I. Pyun and T.-H. Yang, *J. Electroanal. Chem.*, **441**, 183 (1998).